INTERNATIONAL JOURNAL FOR NUMERICAL AND ANALYTICAL METHODS IN GEOMECHANICS
Int. J. Numer. Anal. Meth. Geomech. 2008; **32**:1147–1172

Random porosity fields and their influence on the stability of granular media

José E. Andrade[1,*,†], Jack W. Baker[2] and Kirk C. Ellison[1]

[1]*Department of Civil and Environmental Engineering, Northwestern University, Evanston, IL 60208, U.S.A.*
[2]*Department of Civil and Environmental Engineering, Stanford University, Stanford, CA 94305, U.S.A.*

SUMMARY

It is well established that the mechanical behavior of granular media is strongly influenced by the media's microstructure. In this work, the influence of the microstructure is studied by integrating advances in the areas of geostatistics and computational plasticity, by spatially varying the porosity on samples of sand. In particular, geostatistical tools are used to characterize and simulate random porosity fields that are then fed into a nonlinear finite element model. The underlying effective mechanical response of the granular medium is governed by a newly developed elastoplastic model for sands, which readily incorporates spatial variability in the porosity field at the meso-scale. The objective of this study is to assess the influence of heterogeneities in the porosity field on the stability of sand samples. One hundred and fifty isotropic and anisotropic samples of dense sand are failed under plane-strain compression tests using Monte Carlo techniques. Results from parametric studies indicate that the axial strength of a specimen is affected by both the degree and orientation of anisotropy in heterogeneous porosity values with anisotropy orientation having a dominant effect, especially when the bands of high porosity are aligned with the natural orientation of shear banding in the specimen. Copyright © 2007 John Wiley & Sons, Ltd.

Received 8 February 2007; Revised 29 May 2007; Accepted 13 June 2007

KEY WORDS: random fields; finite elements; elastoplasticity; granular materials

1. INTRODUCTION

Most geotechnical engineering problems are multi-scale in nature because of inherent or induced inhomogeneities existing at different length scales in geomaterials. Inherent inhomogeneities are defined as those resulting from fluctuations in material properties such as permeability or strength. Induced inhomogeneities are those imposed by a physical phenomenon (e.g. deformation) that alters

---

[*] Correspondence to: José E. Andrade, Department of Civil and Environmental Engineering, Northwestern University, Evanston, IL 60208, U.S.A.
[†] E-mail: j-andrade@northwestern.edu

Contract/grant sponsor: Northwestern University

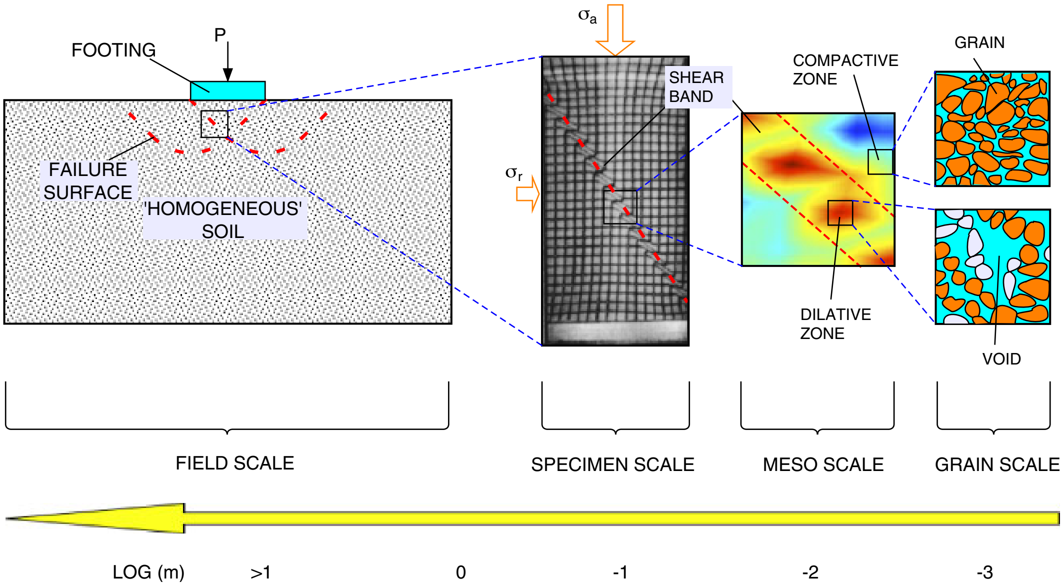

Figure 1. Multi-scale nature of granular materials. Some portions after [1, 2].

the characteristics of the medium. Figure 1 shows typical scales relevant to granular materials. All the information pertaining to granular systems, including inhomogeneities, is encoded at the granular scale and propagated or upscaled through all the way to the field scale. Indeed, the deformation and flow process in granular materials is a multi-scale process.

It is well established that the mechanical behavior and flow properties of granular media are strongly influenced by heterogeneities in the media. Heterogeneities introduce local ‘weaknesses’ that trigger instabilities. For this reason, advanced mechanical models for predicting the onset of instabilities are most useful when coupled with heterogeneous models for granular media. Soil variability can be accounted for by coupling random field theory and numerical tools such as the finite element method [3, 4]. This type of approach has been used to characterize random fields at the ‘site’ scale. For instance, Griffiths and Fenton [5] have studied the impact of fluctuations in strength characteristics in soils in the context of bearing capacity and slope stability. Paice *et al.* [6] have studied the effects of random soil properties on settlements. Here, a newly developed elastoplastic model for sands is coupled with a random field simulator to study the behavior of granular material at the ‘meso’-scale. The meso-scale ($\sim 10^{-2}$ m), as shown in Figure 1, is defined as an intermediate scale between the specimen scale ($\sim 10^{-1}$ m) and the granular scale ($\sim 10^{-3}$ m).

The novel elastoplastic model is based on critical state soil mechanics (CSSM) and introduces a state parameter ψ proposed by Been and Jefferies [7], which controls the dilatancy and hardening/softening behavior of the samples. Because the granular scale is key to the behavior of granular media (see Figure 1), the constitutive model obtains information of the porosity at the meso-scale. Porosity and number of nearest neighbors (coordination number) jointly define fabric in granular materials, which has been shown to control the mechanical behavior of such materials [8], thus realistic models for sands must attempt to capture fabric. One possible way to do so is to explicitly model the material at the granular scale, using the discrete element method [9], but this

DOI: 10.1002/nag

makes the modeling excessively expensive and it is not clear whether the method can simulate accurately the behavior of angular particles such as sands at this point in time. One possible alternative, which we follow herein, is to use continuum models that introduce information from lower scales such as the meso-scale. This meso-scale model has previously been used to simulate the behavior of sands under drained and undrained conditions using a deterministic framework [10–12]. Here, finite element models are constructed to simulate the behavior of dense sands under plane-strain loading under drained conditions. The objective of the study is to couple the mechanical model (finite element model) with a stochastic model (using Monte Carlo simulations) to systematically study the impact of inhomogeneities and anisotropies in the stability of plane-strain samples of dense sands.

Monte Carlo simulations of random porosity fields are generated and used as input to the mechanical model. Simulations are generated for anisotropic fields, varying both the degree and orientation of anisotropy. Coupling of random fields with finite element soil models is a relatively well-studied problem, and a number of researchers have developed proposals for efficient simulation [13, 14]. Here, methods developed in the field of Geostatistics are used [15]. This approach, which relies on a series of conditional simulations of soil properties over the spatial domain of the specimen, is chosen because of its simple interface with experimental data. Experiments can be used to characterize the stochastic properties of the random fields, and conditional simulations of specimens can be performed in the case where properties are measured in a few locations and unknown in other locations. No coupling with experimental data is performed here; rather, a parametric study of the effect of random field properties is used to identify the sensitivity of instability behavior to variations in the underlying porosity field. The future extension of the work to incorporate experimental data for calibration and validation of the model will thus be a natural one.

An outline of the paper is as follows. A mechanical model for granular media is first described in detail. The model for performing Monte Carlo simulations of porosity fields is then described, and the results are used as input for finite element analyses of drained sand specimens. The finite element analysis results are then summarized and systematic trends are identified. The relationship between the axial compressive strength of a specimen and the degree and orientation of anisotropy in heterogeneous porosity values is investigated. Of particular interest is the orientation of anisotropies in the specimen, in relation to the natural orientation of shear banding caused by the loading.

As for notations and symbols used in this paper, bold-faced letters denote tensors and vectors; the symbol '$\cdot$' denotes an inner product of two vectors (e.g. $\mathbf{a} \cdot \mathbf{b} = a_i b_i$), or a single contraction of adjacent indices of two tensors (e.g. $\mathbf{c} \cdot \mathbf{d} = c_{ij} d_{jk}$); the symbol ':' denotes an inner product of two second-order tensors (e.g. $\mathbf{c} : \mathbf{d} = c_{ij} d_{ij}$), or a double contraction of adjacent indices of tensors of rank two and higher (e.g. $\mathbf{C} : \boldsymbol{\varepsilon}^{\mathrm{e}} = C_{ijkl} \varepsilon^{\mathrm{e}}_{kl}$); the symbol '$\otimes$' denotes a juxtaposition, e.g. $(\mathbf{a} \otimes \mathbf{b})_{ij} = a_i b_j$. Finally, for any symmetric second-order tensors $\boldsymbol{\alpha}$ and $\boldsymbol{\beta}$, $(\boldsymbol{\alpha} \otimes \boldsymbol{\beta})_{ijkl} = \alpha_{ij} \beta_{kl}$, $(\boldsymbol{\alpha} \oplus \boldsymbol{\beta})_{ijkl} = \beta_{ik} \alpha_{jl}$, and $(\boldsymbol{\alpha} \ominus \boldsymbol{\beta})_{ijkl} = \alpha_{il} \beta_{jk}$.

2. MECHANICAL MODEL: CONSTITUTIVE MODEL FOR SANDS

It is well documented in the literature that the mechanical behavior of granular materials is governed by the coordination number and the forces applied at the contact points at each grain. Unfortunately, current models (and computational power) do not allow us to look at the grain scale to simulate

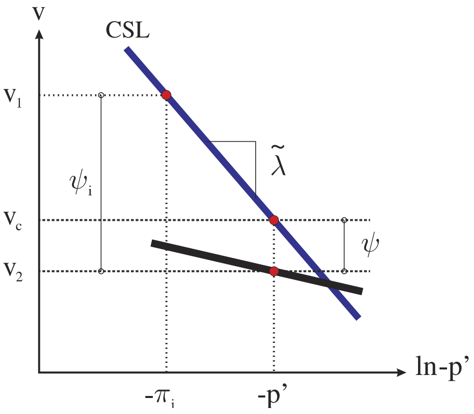

Figure 2. Geometric representation of the state parameter ψ.

the behavior of assemblies of grains as in the case of sands. One possible alternative is to develop macroscopic models that can include fine-scale details key for the behavior of granular bodies. A recently developed model for sands includes information about the relative density at a point in the sample *via* the state parameter ψ [11, 12]. The state parameter ψ was first introduced by Been and Jefferies [7] to quantify the distance, in specific volume, v, from the critical state at a certain mean normal stress. Hence, the state parameter serves to better quantify the behavior of sands relative to their density and consequently has been used in the development of plasticity models (see, for example, [11, 12, 16, 17]). A geometrical interpretation for ψ is shown in Figure 2. Depending on the sign of the state parameter, a material point is said to be denser than critical (below the critical state line (CSL), $\psi<0$) or looser than critical (above CSL, $\psi>0$). It is well known that the load–displacement and dilatancy of sand samples are sharply distinct depending on whether the samples are loose or dense. Hence, the state parameter is key to capturing the behavior of sands accurately.

In this paper, we use the model developed by Andrade and Borja [11] and Borja and Andrade [12] to study the effect of structured specific volume fields across specimens of dense sands (i.e. $\psi<0$ on average). Here, we summarize some of the most salient features of the infinitesimal model for completeness and clarity of presentation. The interested reader is referred to [11, 12] for details regarding the elastoplastic model under small and large strains and their respective numerical implementation. However, all the numerical results presented herein are obtained using the finite deformation theory. The elastic response of the model is hyperelastic and thus governed by a stored energy density function $\Psi^e(\boldsymbol{\varepsilon}^e)$ such that the effective stress tensor is given by

$$\boldsymbol{\sigma}' = \frac{\partial \Psi^e}{\partial \boldsymbol{\varepsilon}^e} \tag{1}$$

where the stored energy is an isotropic function of the elastic strain tensor $\boldsymbol{\varepsilon}^e$. The total stress tensor $\boldsymbol{\sigma}$ is decomposed according to Terzaghi's well-known expression for fully saturated soils i.e. $\boldsymbol{\sigma} = \boldsymbol{\sigma}' - p\boldsymbol{\delta}$, where p is the pore fluid pressure and is negative under compression, following continuum mechanics convention. The tensor $\boldsymbol{\delta}$ is the second-order identity.

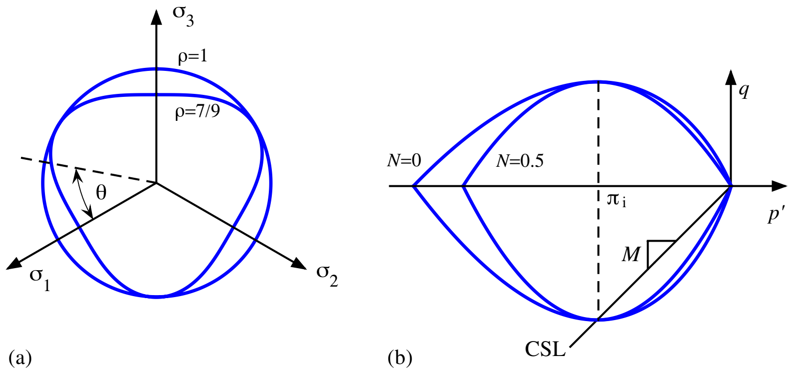

Figure 3. Three invariant yield surface on (a) deviatoric plane at different values of ϱ and (b) meridian plane at different values of N.

Let us define three independent invariants for the effective stress tensor $\boldsymbol{\sigma}'$,

$$p' = \frac{1}{3}\operatorname{tr}\boldsymbol{\sigma}', \quad q = \sqrt{\frac{2}{3}}\|\mathbf{s}'\|, \quad \frac{1}{\sqrt{6}}\cos 3\theta = \frac{\operatorname{tr}\mathbf{s}'^3}{\chi^3} \tag{2}$$

where $\mathbf{s}' = \boldsymbol{\sigma}' - p'\boldsymbol{\delta}$ is the deviatoric component of the effective stress tensor, and $\chi = \sqrt{\operatorname{tr}\mathbf{s}'^2}$. The invariant p' is the mean normal effective stress and is assumed to be negative throughout. Further, θ is the so-called Lode's angle whose values are in the range $0 \leqslant \theta \leqslant \pi/3$; it defines an angle emanating from a tension corner on a deviatoric plane (see Figure 3).

The elastic region in effective stress space is contained by the yield surface which is a function of the three stress invariants introduced above,

$$F(\boldsymbol{\sigma}', \pi_i) = F(p', q, \theta, \pi_i) = \zeta(\theta)q + p'\eta(p', \pi_i) \tag{3}$$

with

$$\eta = \begin{cases} M[1 + \ln(\pi_i/p')] & \text{if } N = 0 \\ M/N[1 - (1-N)(p'/\pi_i)^{N/(1-N)}] & \text{if } N > 0 \end{cases} \tag{4}$$

The function ζ controls the cross-sectional shape of the yield function on a deviatoric plane as a function of the Lode's angle. We adopt the shape function proposed by Argyris *et al.* [18] and Gudehus [19] because of its mathematical simplicity, i.e.

$$\zeta(\theta) = \frac{(1+\varrho) + (1-\varrho)\cos 3\theta}{2\varrho} \tag{5}$$

where as shown in Figure 3, the ellipticity constant ϱ controls the form of the cross-section going from perfectly circular $\varrho = 1$ to convex triangular for $\varrho = 7/9$. The shape function with $\varrho < 1$ reflects a classical feature in geomaterials, which exhibit higher strength in triaxial compression. Figure 3 also reflects the geometrical interpretation for parameters M and N which govern the slope of the CSL and the curvature of the yield surface on a meridian plane, respectively.

DOI: 10.1002/nag

Central to the formulation is the additive decomposition of the strain rate tensor into elastic and plastic parts

$$\dot{\boldsymbol{\varepsilon}} = \dot{\boldsymbol{\varepsilon}}^{\mathrm{e}} + \dot{\boldsymbol{\varepsilon}}^{\mathrm{p}} \tag{6}$$

with the plastic component given by the non-associative flow rule

$$\dot{\boldsymbol{\varepsilon}}^{\mathrm{p}} = \dot{\lambda}\frac{\partial G}{\partial \boldsymbol{\sigma}'} \tag{7}$$

where the scalar $\dot{\lambda}$ is the so-called plastic multiplier giving the 'magnitude' of plastic deformation. The plastic potential function G is postulated as form identical to the yield surface i.e.

$$G(\boldsymbol{\sigma}', \overline{\pi}_{\mathrm{i}}) = G(p', q, \theta, \overline{\pi}_{\mathrm{i}}) = \zeta(\theta)q + p'\overline{\eta}(p', \overline{\pi}_{\mathrm{i}}) \tag{8}$$

where

$$\overline{\eta} = \begin{cases} M[1 + \ln(\overline{\pi}_{\mathrm{i}}/p')] & \text{if } \overline{N} = 0 \\ M/\overline{N}[1 - (1 - \overline{N})(p'/\overline{\pi}_{\mathrm{i}})^{\overline{N}/(1-\overline{N})}] & \text{if } \overline{N} > 0 \end{cases} \tag{9}$$

When the size parameter $\overline{\pi}_{\mathrm{i}} = \pi_{\mathrm{i}}$ and the curvature constant $\overline{N} = N$, then plastic flow is associative, otherwise, there is volumetric nonassociativity of plastic flow.

As mentioned earlier, the model is based on CSSM [20]. In these classical models, the image stress π_{i} coincides with the critical state or the CSL. To apply the model to sands, which exhibit different types of volumetric yielding depending on initial density, the yield surface is detached from the critical state line along the v-axis. Thus, the state point (v, p', q) may now lie either above or below the critical specific volume v_{c} (see Figure 2) at the same stress p' depending on whether the sand is looser or denser than critical. Further, a state parameter ψ_{i} is introduced denoting the distance of the same current state point to $v_{\mathrm{c,i}}$ on the CSL at $p' = \pi_{\mathrm{i}}$. The relation between ψ and ψ_{i} is

$$\psi_{\mathrm{i}} = \psi + \tilde{\lambda}\ln\left(\frac{\pi_{\mathrm{i}}}{p'}\right) \tag{10}$$

Hence, ψ is negative below the CSL and positive above it. An upshot of disconnecting the yield surface from the CSL is that it is no longer possible to locate a state point on the yield surface by prescribing p' and q alone: one also needs to specify the state parameter ψ to completely describe the state of a point. Furthermore, isochoric plastic flow does not occur only on the CSL anymore, but could also take place at the image stress point. Finally, the parameter ψ_{i} dictates the amount of plastic dilatancy in the case of dense sands.

Formally, plastic dilatancy is defined by the expression

$$D := \dot{\varepsilon}_{\mathrm{v}}^{\mathrm{p}}/\dot{\varepsilon}_{\mathrm{s}}^{\mathrm{p}} = \frac{\eta - M}{1 - \overline{N}} \tag{11}$$

where, $\dot{\varepsilon}_{\mathrm{v}}^{\mathrm{p}}$ and $\dot{\varepsilon}_{\mathrm{s}}^{\mathrm{p}}$ are the volumetric and deviatoric invariants of the plastic strain rate, respectively. This definition is valid for all possible values of η, even for $\eta = 0$ where Q is not a smooth function. However, experimental evidence on a variety of sands suggests that there exists a maximum possible plastic dilatancy, D^*, which limits a plastic hardening response. The value of D^* depends on the state parameter ψ_{i}, increasing in value as the state point lies farther and farther away from the CSL on the dense side. An empirical correlation has been established experimentally in [16] between the plastic dilatancy D^* and the state parameter ψ_{i}, and takes the form $D^* = \alpha\psi_{\mathrm{i}}$ where $\alpha \approx -3.5$ for most sands. The corresponding size of the yield surface is

$$\frac{\pi_{\mathrm{i}}^*}{p'} = \begin{cases} \exp(\overline{\alpha}\psi_{\mathrm{i}}/M) & \text{if } \overline{N} = N = 0 \\ (1 - \overline{\alpha}\psi_{\mathrm{i}} N/M)^{(N-1)/N} & \text{if } 0 \leqslant \overline{N} \leqslant N \neq 0 \end{cases} \tag{12}$$

where

$$\overline{\alpha}\beta = \alpha, \quad \beta = \frac{1-N}{1-\overline{N}} \tag{13}$$

In the above expression, we have introduced a non-associativity parameter $\beta \leqslant 1$, where $\beta = 1$ in the associative case.

For elastoplastic response, the standard consistency condition on the yield function results in a hardening law given by the equation

$$\dot{\pi}_{\mathrm{i}} = h(\pi_{\mathrm{i}}^* - \pi_{\mathrm{i}})\dot{\varepsilon}_s^{\mathrm{p}} \tag{14}$$

where h is a hardening material constant. Since $h > 0$ and $\dot{\varepsilon}_s^{\mathrm{p}} > 0$, the sign of $\dot{\pi}_{\mathrm{i}}$, controlling the evolution of the yield surface depends on the sign of $(\pi_{\mathrm{i}}^* - \pi_{\mathrm{i}})$: the yield surface expands if $\pi_{\mathrm{i}}^* < \pi_{\mathrm{i}}$ (hardening), the yield surface contracts if $\pi_{\mathrm{i}}^* > \pi_{\mathrm{i}}$ (softening), the size of the yield surface remains unchanged if $\pi_{\mathrm{i}}^* = \pi_{\mathrm{i}}$ (perfect plasticity). In classical Cam–Clay theory, the evolution of the yield surface depends on the sign of $\dot{\varepsilon}_{\mathrm{v}}^{\mathrm{p}}$, i.e. the yield surface expands under compaction and contracts under dilation. However, as noted above, this simple criterion does not adequately capture the hardening/softening responses of sands, which are shown to be dependent on the limit hardening plastic dilatancy D^*, i.e. yield surface expansion if $D < D^*$ and contraction if $D > D^*$.

3. CHARACTERIZATION AND SIMULATION OF MATERIAL PROPERTIES

A series of numerical examples will be used in conjunction with the above modeling technique to assess the effect of several types of material inhomogeneities. The porosity fields are specified as random but with spatial structure. Once the fields have been defined appropriately, Monte Carlo simulations are created and used as input for the above mechanical models. Details regarding the characterization and simulation of random fields are provided in the following section.

3.1. Distribution of void ratio values

Void ratio, ϕ^{f}, is the material parameter being explicitly modeled as random. Thus, void ratio values are modeled as random variables taking values between 0.55 and 0.65, with a mean value of 0.57 (this mean value of void ratio corresponds to that used in [21] to study the strength of dense sands). An exponential probability distribution is used, based on the findings of Shahinpoor [22], and a shift and truncation of the basic exponential distribution is used to provide the appropriate mean value and range of void ratio values. This distribution can be described using as a probability

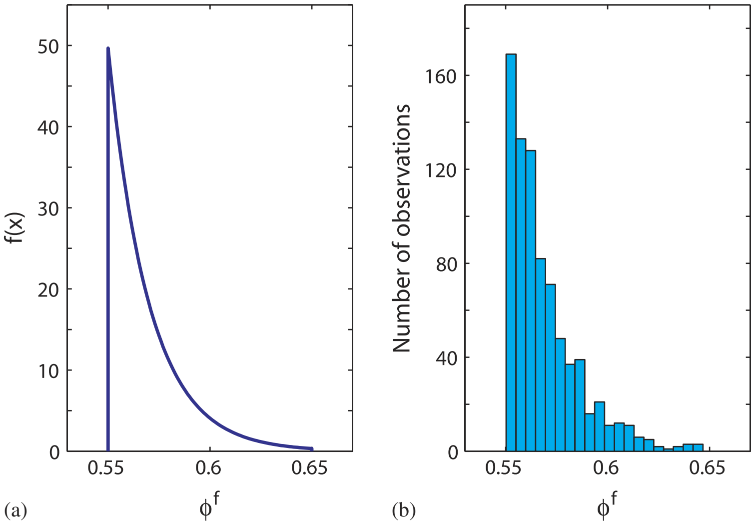

Figure 4. (a) Probability density function for void ratio values. (b) Histogram of void ratio values from a single simulation.

density function (PDF):

$$f(x) = \frac{P(x \leqslant \phi^{\mathrm{f}} < x + \mathrm{d}x)}{\mathrm{d}x} = \begin{cases} 49.66\mathrm{e}^{-50(x-0.55)} & \text{if } 0.55 \leqslant x < 0.65 \\ 0 & \text{otherwise} \end{cases} \tag{15}$$

where, following typical random variable notation, $f(\square)$ has been used to denote the PDF. By integrating this function over the appropriate bounds, the cumulative distribution function (CDF) for ϕ^{f} is obtained

$$F(x) = P(\phi^{\mathrm{f}} < x) = \begin{cases} 0 & \text{if } x \leqslant 0.55 \\ \dfrac{1-\mathrm{e}^{-50(x-0.55)}}{1-\mathrm{e}^{-50(0.1)}} & \text{if } 0.55 < x \leqslant 0.65 \\ 1 & \text{if } x > 0.65 \end{cases} \tag{16}$$

where $F(\square)$ is used to denote the CDF.

A plot of the PDF from Equation (15) is shown in Figure 4(a). The ϕ^{f} values associated with large $f(x)$ values (i.e. those equal to or slightly larger than 0.55) are those most likely to occur when simulations are performed. For comparison, a histogram of simulated ϕ^{f} values from one of the simulations below is shown in Figure 4(b). This histogram has the same general shape as the PDF, but because the simulation consists of only a finite number of random samples from this distribution, there will be some variation and the two will not match exactly. Implications of this will be discussed later.

3.2. *Spatial dependence*

The probabilistic model of the previous section describes the distribution of void ratio values at single locations; once porosity values are considered within a 'laboratory' specimen (see Figure 1 for relative scale), these values are treated as spatially correlated random variables. That is, porosity values at individual locations will vary from simulation to simulation, but in a manner that exhibits spatial structure at the meso-scale. Although, at larger scales, porosity values can be modeled as decreasing systematically with increasing depth [23], at the scale of interest here it is appropriate to assume no trend in mean values or distributions of porosity. This condition is termed stationarity in random field literature, and slightly simplifies the calculations below.

The stochastic dependence between porosity values at any two points is modeled using a covariance function. For variables having a multivariate Gaussian probability distribution, this fully describes the joint dependence between values at two points, and the analytical equations are very tractable. Void ratio does not seem to have a Gaussian distribution [22], however, and stochastic dependence among variables having the exponential distribution given by Equation (15) is not fully defined by a covariance. To take advantage of the desirable property of multivariate Gaussian models, the data of interest are transformed using a normal-score mapping. First spatially dependent Gaussian random fields are simulated, and then each value of the Gaussian field is mapped into the target probability distribution using the relationship

$$x = F^{-1}(\Phi(z)) \tag{17}$$

where x is the ϕ^{f} data having the target distribution, $F^{-1}(\Box)$ is the inverse of the CDF given in Equation (16), $\Phi(\Box)$ is the CDF of the standard Gaussian distribution and z is one value from the simulated Gaussian data. This transformation yields x values with the proper distribution if z comes from the standard Gaussian distribution. With the proper marginal distribution accounted for by this transformation, it is sufficient to simulate standard Gaussian fields.

Spatial dependence of the Gaussian random field is characterized using the semicovariance, in the form of a semivariogram [15]. The semivariogram, denoted $\gamma(\mathbf{h})$, is equal to half of the variance of the increment in data points separated by a distance $\mathbf{h}$

$$\gamma(\mathbf{h}) = \tfrac{1}{2}\mathrm{Var}[Z(\mathbf{u}) - Z(\mathbf{u}+\mathbf{h})] \tag{18}$$

where $Z(\mathbf{u})$ is the distribution of the Gaussian random variable at location $\mathbf{u}$. Note that an upper-case Z is used to denote an uncertain quantity (i.e. a random variable), and a lower-case z is used in Equation (17) to denote a specific numerical value taken by the random variable Z. The vector distance $\mathbf{h}$ accounts for both separation length and direction. Note that this is the variance of the underlying Gaussian distributed variables rather than the variables having the final target distribution. This semivariogram is often used in geostatistics instead of a covariance because it requires second-order stationarity of only the increments and not the underlying process, but here and in many other cases the two can be used interchangeably. Tools for estimating semivariograms using experimental data are available in many GIS software packages, as well as stand-alone packages (e.g. [24]).

In the examples below, a semivariogram of the following form is used:

$$\gamma(\mathbf{h}) = \begin{cases} \dfrac{3}{2}\left(\left(\dfrac{h_1}{a}\right)^2 + \left(\dfrac{h_2}{b}\right)^2\right)^{1/2} - \dfrac{1}{2}\left(\left(\dfrac{h_1}{a}\right)^2 + \left(\dfrac{h_2}{b}\right)^2\right)^{3/2} & \text{if } \left(\dfrac{h_1}{a}\right)^2 + \left(\dfrac{h_2}{b}\right)^2 \leqslant 1 \\ 1 & \text{if } \left(\dfrac{h_1}{a}\right)^2 + \left(\dfrac{h_2}{b}\right)^2 > 1 \end{cases} \tag{19}$$

where h_1 and h_2 are the scalar distances along the field's major and minor axes, respectively, corresponding to the vector distance $\mathbf{h}$. This function is termed a spherical semivariogram in the Geostatistics literature. The parameters a and b specify how quickly the spatial dependence decreases with increasing separation distance between the points of interest. This functional form is commonly used for modeling spatially dependent phenomena [15], and the simulations using this model (shown below) are reasonable representations of realistic porosity values, but a few other functional forms can be substituted here if future data suggest that an alternate model is more appropriate. In this model, if $a=b$, then the random field is isotropic. For results below, an 'anisotropy ratio', a/b, is provided to indicate the degree of anisotropy in the field. The angle of the major axis with respect to the horizontal is also given. To ensure that the fields with differing anisotropy ratios have correlation structure at approximately the same scale, a and b are chosen such that $a \times b$ is approximately constant for all simulations.

It is important to note that the semivariogram model of Equation (19) is describing the Gaussian variables z, rather than the void ratio values x obtained using Equation (17). The covariance structures of the two are often similar, especially if the transformed distribution is similar to the original Gaussian distribution [25, 26]. Here, the transformed random variable is not similar to the Gaussian distribution, so a further check was performed to investigate any potential significant differences. Empirical semicovariances were computed for one set of simulated data, both before and after the transformation, and the results are compared with the originally specified semivariogram in Figure 5. Results are shown for an isotropic case, so that the semivariogram is a function of only the separation distance (and not the orientation). The empirical semivariograms for the original and transformed data are surprisingly similar. Note that the slight difference between the specified semivariogram and observed result for the non-transformed data is due to the finite sample size. While the finite area (relative to the correlation length) used to perform the estimation limits causes some difference between the observed and specified semivariogram, the high resolution within that area causes the empirical semivariogram to vary smoothly, unlike typical results from more sparsely sampled measured data. This smooth variation does not mean that the sample area is large enough to have converged to the specified semivariogram, as can be seen in the figure. The results from Figure 5 suggest that in this specific case the semivariogram can be interpreted as the semivariogram for the transformed data, but this will not be true generally. This is an important consideration if the semivariogram is to be estimated from experimental data.

Once spatial dependence of the Gaussian random field has been defined, realizations of porosity can be generated using a sequential simulation approach. A series of 20×40 grids of porosity values are desired for input into the mechanical model described above. Thus, a set of simulated joint realizations of void ratio values are needed for these 800 elements, consistent with the above stochastic model.

It is straightforward to directly simulate the needed spatially dependent Gaussian field, but here a sequential conditional simulation approach is used. The proposed approach is only slightly more complex than a direct simulation, but is more flexible because it can allow incorporation of measurements at some locations. While measurements are not incorporated here, it is a natural future extension of the proposed framework.

To perform a sequential conditional simulation, first an arbitrary location in the grid is selected and a simulation is generated from the standard Gaussian distribution. For each following step, an arbitrary unsampled location is chosen, and a simulation is generated, conditional on values of the previously simulated data point(s). Because the field is Gaussian, the needed conditional distribution is easy to compute. Let $Z^{(i)}$ denote the random field value at unsampled location $\mathbf{u}^{(i)}$,

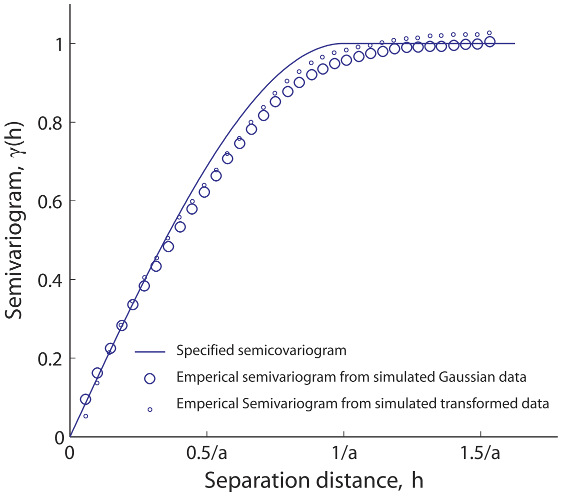

Figure 5. Specified and empirical semivarigrams for one simulation of the isotropic void ratio field.

and $\mathbf{Z}^{(\text{sampled})}$ denote the random field values at previously simulated locations $\mathbf{u}^{(\text{sampled})}$. The joint distribution of $Z^{(i)}$ and $\mathbf{Z}^{(\text{sampled})}$ is given by

$$\left[\frac{Z^{(i)}}{\mathbf{Z}^{(\text{sampled})}}\right] \sim N\left(\left[\begin{array}{c}0\\ \hline \mathbf{0}\end{array}\right], \left[\begin{array}{c|c}1 & \mathbf{\Sigma}_{12}\\ \hline \mathbf{\Sigma}_{21} & \mathbf{\Sigma}_{22}\end{array}\right]\right) \tag{20}$$

where $\sim N(\boldsymbol{\mu}, \mathbf{\Sigma})$ denotes that the vector of random variables has a joint normal distribution with mean values $\boldsymbol{\mu}$ and covariance matrix $\mathbf{\Sigma}$ (note that $\boldsymbol{\mu}$ and $\mathbf{\Sigma}$ have been partitioned in Equation (20), to clarify the matrix operations below). The vector $\mathbf{Z}^{(\text{sampled})}$ represents the data values at the previously simulated locations, and $\mathbf{0}$ is a vector of zeros having the same size as $\mathbf{Z}^{(\text{sampled})}$ (i.e. the mean vector, which is equal to zero because $\mathbf{Z}$ is standardized). The covariance matrix is dependent on the locations of the previously simulated data points; each element of the matrix can be computed by evaluating Equation (19) and using the property that the covariance between locations with separation distance $\mathbf{h}$ is equal to $1-\gamma(\mathbf{h})$. Note that all variances are equal to one because the field is standardized.

Given this model, the distribution of $Z^{(i)}$ conditional upon the original data points is given by

$$(Z^{(i)}|\mathbf{Z}^{(\text{sampled})} = \mathbf{z}) \sim N(\mathbf{\Sigma}_{12}\cdot\mathbf{\Sigma}_{22}^{-1}\cdot\mathbf{z},\, 1-\mathbf{\Sigma}_{12}\cdot\mathbf{\Sigma}_{22}^{-1}\cdot\mathbf{\Sigma}_{21}) \tag{21}$$

where $\mathbf{z}$ is the vector of previously simulated numerical values. Note that $\mathbf{Z}^{(\cdot)}$ is a random variable representing the model for uncertain porosities prior to simulation; the numerical values $\mathbf{z}$ were obtained in the previous steps of the simulation. A value for $Z^{(i)}$ is simulated from this conditional distribution, and this value is then treated as a fixed data point for later simulations at other locations (i.e. $Z^{(i)}$ is included in the vector $\mathbf{Z}^{(\text{sampled})}$ of Equation (21)). The conditional simulation process is repeated until all values in the field have been simulated.

Each value in the resulting simulated field is then transformed using Equation (17), and the resulting transformed field has the target probability distribution for void ratio values. Each

Table I. Summary of simulations performed showing anisotropy ratios, orientations, and mesh resolution.

		Number of simulations		
a/b	Orientation	20×40	20×40 normalized	10×20
1	n.a.	12	1	1
10	0	12	1	—
10	30	12	1	—
10	45	12	1	—
10	60	12	1	—
10	90	12	1	—
100	0	12	1	1
100	30	12	1	1
100	45	12	1	1
100	60	12	1	1
100	90	12	1	1

simulation obtained in this manner represents one potential realization of void ratio values at the meso-scale. Example simulated fields obtained using this method are shown in Figure 8.

3.3. *Simulating random fields*

A series of simulations were performed using the above random fields simulation approach. To assess the influence of various porosity field properties on the stability of sand samples, simulations were performed for a range of conditions. It was expected that the degree of anisotropy of the sample and the orientation of the anisotropy would have significant effects on sample stability, so these properties were varied parametrically and several simulations were generated for each set of parameter values. The parameter values considered are summarized in Table I.

The random field simulations vary within the specimen, but mean porosity values associated with each specimen also vary from simulation to simulation. This is expected given the stochastic model described above, but the specimen-to-specimen variability in mechanical behavior induced by these variations makes it more difficult to compare trends due to variation in the degree and orientation of anisotropy. To address this challenge, another set of simulations was performed, but the porosity values from this second set of simulations were normalized so that the mean and standard deviation of porosity values within each Monte Carlo simulation was constant. Later, instability results will be shown for both the normalized and non-normalized simulations, to demonstrate the value of this normalization.

3.4. *Calibration with experimental data*

The approach described above can easily utilize experimental data for two purposes: to determine an appropriate probability distribution and spatial correlation function for ϕ^{f}, or to incorporate measured porosity values into simulations of a specimen that includes some unmeasured locations.

To determine an appropriate probability distribution, one can use methods of statistical inference. Void ratio measurements taken at many locations in a sample can be used to generate a histogram analogous to that shown in Figure 4(b). The data can be used to estimate the mean and standard

DOI: 10.1002/nag

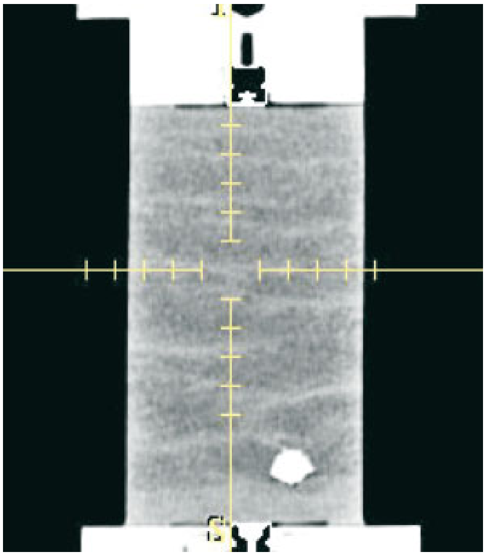

Figure 6. Cross-section through a biaxial test specimen of silica sand analyzed by X-ray computed tomography, white spot is a piece of gravel (after [12], courtesy of Prof. A. Rechenmacher).

deviation of porosity in that sample, and a PDF can be chosen to represent the complete histogram (e.g. [27]). Given a sufficient number of void ratio measurements, the PDF of Equation (15) could thus be refined to represent the particular material being studied. While this calibration is not a focus of the present manuscript, it is a well-developed approach that is simple to incorporate within the framework described here. One source of data that could be used for calibration at the meso-scale is X-ray tomography. Figure 6 shows example results obtained using this method. By converting this graphical data to numerical values of properties such as density, and then creating a histogram of these values, one can fit a PDF to use as a replacement for Equation (15). The same data can be used to develop an empirical estimate of the semivariogram defined by Equation (18). Empirical semivariograms are generated by observing differences in pairs of void ratio values, as a function of separation distance and orientation. Sample variances of these paired differences provide a direct estimate of a semivariogram that could be used to replace the one given in Equation (18) [15].

The above framework can also incorporate measured values of ϕ^{f} when performing simulations. This is done by inputting the measured values into the Gaussian field (after back-transforming the data by inverting Equation (17)), and then treating the measured values as if they were previously simulated, when using Equation (20) to simulate values at the remaining locations. That is, the measured values will be included in $\mathbf{Z}^{(\text{sampled})}$ in Equation (20) for simulations at all unsample locations. The resulting simulated field will always agree with observed values at sampled locations, and at other locations it will be consistent with the specified stochastic properties of the field. The ease of incorporating measurements using this approach is one reason why it was proposed above. Incorporation of measurements has been shown to be useful for macro-scale granular media instability problems (e.g. [28]). The approach has not yet been applied to meso-scale problems, but its tractability is appealing.

4. NUMERICAL SIMULATIONS

In this section, we use the above-described framework for coupling an accurate mechanical model for sands with Monte Carlo simulations. The numerical model treats the porosity as a spatially correlated random variable. Plane-strain compression in samples of dense sand are simulated after the mechanical model has been calibrated using experimental data. The objective of the plane-strain simulations is to highlight the importance of meso-scale inhomogeneities. In particular, the effect of anisotropy in the porosity is systematically studied. Anisotropy ratios and orientation of the anisotropy principal axis are systematically varied to study their effect on the stability of dense sand samples under plane-strain compression. Table I gives the different anisotropy ratios and principal axis orientations considered in this paper as well as the number of simulations performed at different mesh resolutions. All simulations performed in this section pertain to samples of macroscopically dense samples (i.e. even inhomogeneous samples are still dense on average).

4.1. Calibration of the constitutive model

In order to perform accurate predictions and to demonstrate the validity of the proposed model for sands, we present some calibration and prediction results based on experimental results obtained by Cornforth [21]. The constitutive model used here is calibrated for Brasted sand under ‘perfectly homogeneous’ conditions based on drained triaxial compression results. Then, the same sand, at the same initial state, is failed numerically and experimentally under plane-strain conditions to confirm the adequacy of the calibration. All the material parameters obtained in the calibration step (under triaxial compression) are kept constant for the prediction phase (under plane-strain compression). This set of experiments provides a true calibration/prediction set since the triaxial compression and plane strain tests were conducted at the same initial state. The only difference is introduced by the different boundary conditions imposed.

The triaxial compression tests were performed on loose and dense samples with void ratios $e=0.754$ and 0.570, coefficients of lateral earth pressure $K_0=0.447$ and 0.381 and initial vertical pressures, $p_0=-390$ and $-426\,\text{kPa}$, respectively. This testing pair was used to determine density-independent hyperelastic and plastic parameters that could be fit to the data in order to reproduce accurate plots of axial strain *versus* deviator stress and axial strain *versus* volumetric strain. Density-specific parameters, including the size of the initial yield surface, π_{i}, and the hardening coefficient, h (see Section 2), were allowed to differ between the loose and dense samples.

The predictive ability of the model was verified using the parameters developed from triaxial compression testing to predict the behavior for identically consolidated samples under plane-strain loading conditions. Plots of principal stresses *versus* axial strain and volumetric strain *versus* axial strain generated by the constitutive model and experimental data are superimposed in Figure 7 for the plane-strain test on dense Brasted sand.

A summary of the testing conditions used to calibrate the model parameters is presented in Table II. Subsequent analysis in this paper will focus on model predictions for anisotropic plane strain testing of dense Brasted sand. The hyperelastic and plastic parameters selected for this sample are presented in Tables III and IV.

4.2. Plane-strain compression simulations

Drained plane-strain simulations on samples of macroscopically dense sand with average specific volume of 1.572 were performed in this section. The main objective of these simulations was

DOI: 10.1002/nag

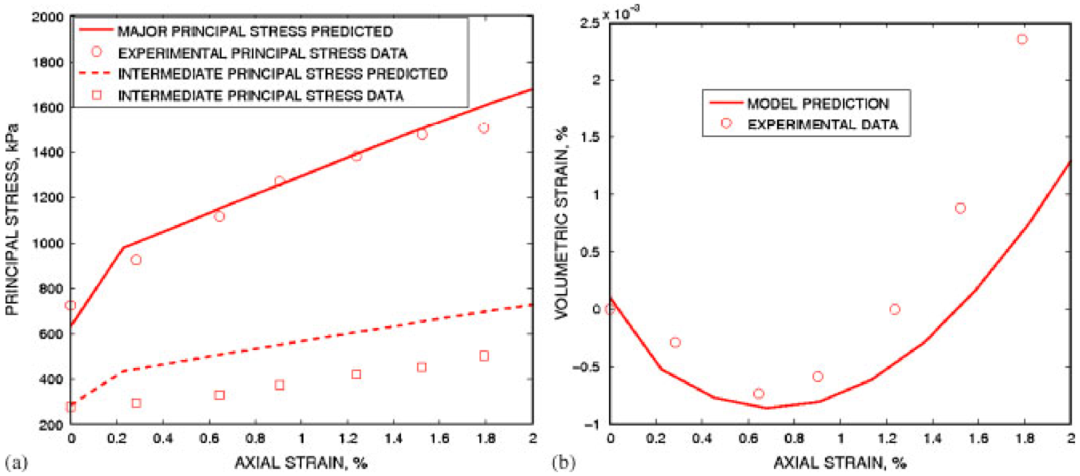

Figure 7. Constitutive model predictions of (a) principal stresses and (b) volumetric strain *versus* axial strain for dense Brasted sand loaded under plane-strain conditions.

Table II. Summary of laboratory tests used to calibrate the constitutive model (from [21]).

Test	e_0	K_0	p_0 (kPa)
Loose			
Triaxial compression	0.754	0.447	390
Plane strain	0.721	0.444	391
Dense			
Triaxial compression	0.570	0.379	426
Plane strain	0.572	0.381	425

Table III. Summary of hyperelastic material parameters for drained plane-strain compression problems.

Symbol	Value	Parameter
$\widetilde{\kappa}$	0.0015	Compressibility
α_0	0	Coupling coefficient
μ_0	45 000 kPa	Shear modulus
p_0	-135 kPa	Reference pressure
$\varepsilon^{\mathrm{e}}_{\mathrm{v}0}$	0	Reference strain

to analyze the impact of anisotropy and its direction on the stability of dense sands. The degree of anisotropy can be measured by the anisotropy ratio a/b (cf. Equation (19), such that $a/b=1$ signifies isotropic conditions, whereas $a/b\neq 1$ would represent anisotropic conditions. As given in Table I, three particular cases were considered herein, $a/b=1$ (isotropic), $a/b=10$, and $a/b=100$. A value of $a/b>1$ indicates a stronger correlation in the principal direction associated with the

DOI: 10.1002/nag

Table IV. Summary of plastic material parameters for drained plane-strain compression problems.

Symbol	Value	Parameter
$\widetilde{\lambda}$	0.02	Compressibility
M	1.27	Critical state parameter
v_{c0}	1.89	Reference specific volume
N	0.4	For yield function
$\overline{N}$	0.4	For plastic potential
ϱ	0.78	Ellipticity
h	120	Hardening coefficient for dense/loose samples

parameter a. Similarly, the principal directions of anisotropy (not to be confused with the principal stress directions) are rotated systematically using the angles $\{0, 30, 45, 60, 90\}$ degrees from the horizontal. Figures 8 and 9 show 'typical' realizations of the initial specific volume for the aforementioned anisotropy ratios and orientations. These figures also show the level of discretization utilized in these simulations, where regular meshes comprised of 20×40 four-node quadrilateral elements were utilized. This fine level of discretization was necessary to capture the gradients in the random porosity field. As mentioned in Section 3.2, realizations for the initial specific volume random field were obtained using a 20×40 grid and hence the finite element resolution is set to match that of the Monte Carlo simulation for the initial porosity. Thus, each finite element represents a region with initially constant porosity. The remaining material parameters required for a full material description are given in Tables III and IV. As mentioned before, these material parameters correspond to a Brasted sand such as that presented in the calibration section and used experimentally in [21]. Incidentally, this constitutive model has also been recently used to capture the behavior of loose sand successfully [29]. In the numerical simulations performed here, all material parameters were treated as constant and deterministic, except for the specific volume. Also, the material parameters chosen reflect an initial anisotropic consolidation ratio $K_0 = 0.381$ in all drained samples.

For the plane-strain simulations presented here, and as shown in Table I, two main sets of random field realizations were performed. The first set of 132 realizations (third column in Table I) consists of non-normalized random field simulations where the initial porosity fields are allowed to have slightly different mean and standard deviation from one sample to another. This then creates a 'sample-to-sample' variability *induced* by the discretization (if we could generate continuum random field realizations, they would have the same mean and standard deviation). The second set of Monte Carlo random field simulations, shown in column 4, correspond to normalized samples with *fixed* sample means and standard deviations. Less variability is expected in the response of these samples since the sample-to-sample variability in mean and standard deviation has been eliminated and the only difference in behavior is due to the anisotropy structure. Realizations of the normalized initial porosity fields are shown in Figures 8 and 9 (i.e. for samples in column 4 in Table I).

The initial stress conditions are anisotropic with an initial axial stress of 225 kPa and initial lateral stress of 90 kPa. Subsequently, the axial stress is increased while the lateral stress is kept constant. The boundary conditions are as follows. The top and bottom faces of the specimens are displacement controlled (Dirichlet B.C.'s) with no vertical displacement on the bottom face and displacement uniformly downward on the top face to replicate smooth platens. Similarly, the

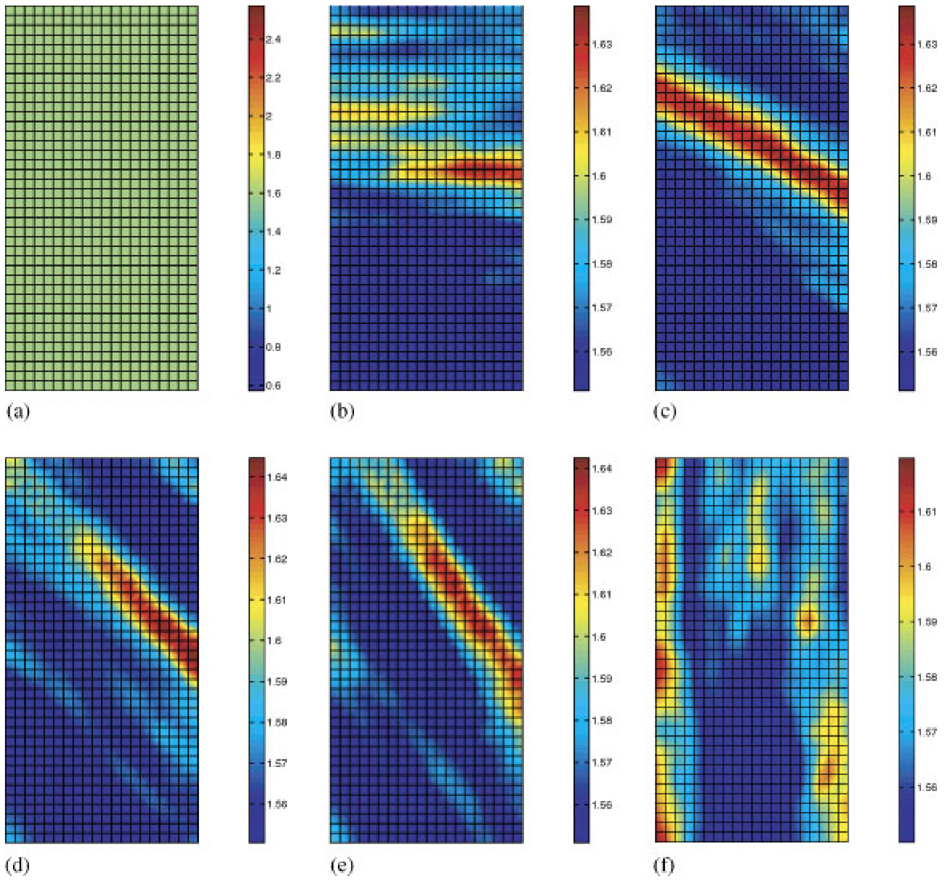

Figure 8. Initial specific volume for samples with anisotropy ratio of 10: (a) homogeneous; (b) principal axis 0°; (c) 30°; (d) 45°; (e) 60°; and (f) 90°.

lateral faces are Neumann B.C.'s where a (constant) lateral confining stress is prescribed. These B.C.'s replicate those of a typical plane-strain compression test in the laboratory.

Figure 10(a) shows the nominal axial stress exerted on the top face of the samples as a function of the nominal axial strain. These responses are plotted for all anisotropic samples as well as for the inhomogeneous, isotropic samples (i.e. $a/b=1$). Additionally, the response from a perfectly homogeneous sample with an initial specific volume of 1.572 is also plotted for comparison. It can be seen in Figure 10 that a wide range of responses is obtained even though the samples have the same macroscopic properties. The anisotropies and inhomogeneities in general yield weaker samples that tend to fail before their homogeneous counterpart does. Failure here is defined as the first instance in which the determinant of the acoustic tensor, as defined in [11, 12], vanishes somewhere in the sample, i.e.

$$\det \mathbf{A} = 0, \qquad \mathbf{A} = \mathbf{n} \cdot \mathbf{c}^{\mathrm{ep}} \cdot \mathbf{n} \tag{22}$$

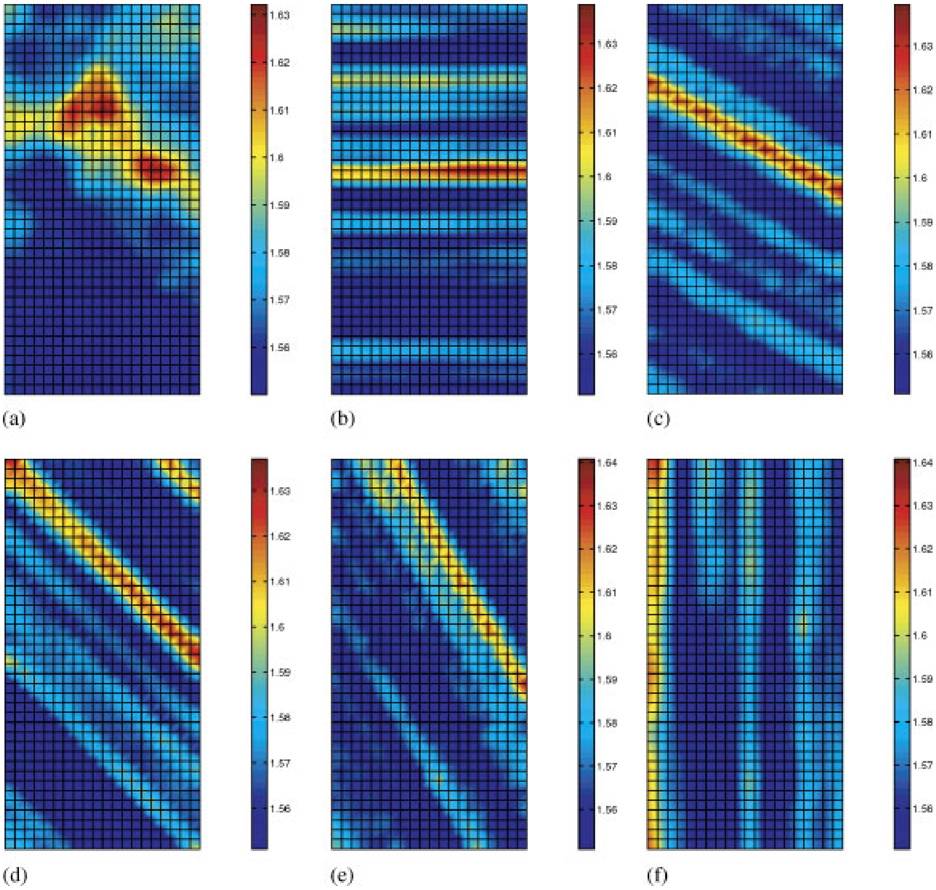

Figure 9. Initial specific volume for samples with anisotropy ratio of 100: (a) isotropic; (b) principal axis 0°; (c) 30°; (d) 45°; (e) 60°; and (f) 90°.

where

$$\dot{\boldsymbol{\sigma}}' = \mathbf{c}^{\mathrm{ep}} : \dot{\boldsymbol{\varepsilon}} \tag{23}$$

and **n** is the normal to the impending shear band. Incidentally, **n** is used here to find the orientation of the impending shear band. Clearly, analyses based on homogeneous samples yield non-conservative strength values. A subset of axial stress *versus* axial strain is shown in Figure 10(b), where only the response of the normalized samples is plotted. We observe that the sample-to-sample variability introduces a spread in the force–displacement curves which is not present in those for the normalized samples. Thus, the sample-to-sample variability in specific volume produces a scatter that is realistic for physical specimens, while the normalization tends to remove that effect. In general, the stress–strain curves for the normalized samples lie on top of each other and on top of the homogeneous response. Only the strength characteristics of the samples differ. Even though the normalized sample results are less scattered, it will be shown that these show the same

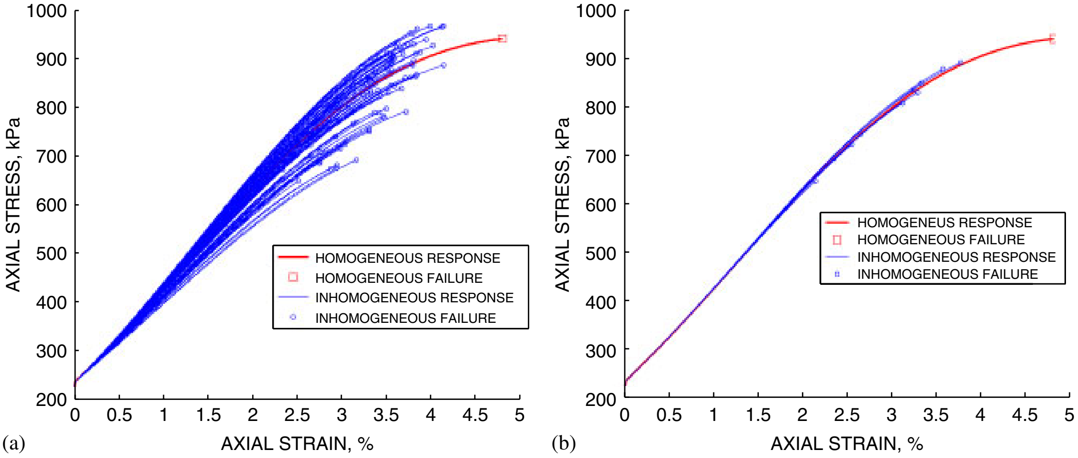

Figure 10. Nominal axial stress for samples of dense sand loaded under drained plane strain: (a) all samples and (b) normalized samples.

trends as their non-normalized counterparts in terms of overall sample strength and the effect of anisotropies.

Figure 11 reports the compressive strength for all non-normalized samples loaded under plane-strain compression. The compressive strength is taken as the axial stress at the moment of failure reported in Figure 10. Figure 11 shows the strengths obtained from all 132 simulations performed at a resolution of 20×40 elements (see Table I), and therefore a clear trend is somewhat difficult to see. For this reason, an average is obtained for each one of the cases studied here: homogeneous, isotropic, anisotropic with $a/b = 10$ and anisotropic with $a/b = 100$. Several observations can be made from these results. First, most samples, except for a rare few, plot below the strength for the homogeneous sample. This clearly shows that inhomogeneities and anisotropies effectively weaken samples. Second, a somewhat surprising result is that the anisotropy ratio tends to increase the overall strength almost everywhere except for the orientations close to 60°. This apparent difference could be due to the fact that longer correlation lengths translate into regions of similar initial porosities, which implies relatively more homogeneous response and hence higher strength. One can picture low correlation lengths implying greater contrast in porosity and hence introducing higher shear stresses. An offsetting effect occurs, however, when the samples with anisotropies have bands of high porosity oriented in approximately the same direction as the expected failure planes (i.e. close to 60°), causing early occurrence of shear localization. This effect is apparent for orientations near 60°, where the $a/b = 100$ case is as strong as the $a/b = 10$ case, but where the isotropic $a/b = 1$ case is the strongest of the three. All these trends were also observed in the results from the normalized samples. These results demonstrate the importance of considering sample heterogeneities when predicting instabilities of granular media.

Remark 1

We note the similarity of these results to those observed in the laboratory and in theoretical analyses of anisotropic rock samples. The trends observed in Figure 11 are qualitatively identical to those reported by McLamore [30] (shown in Figure 12) from theoretical considerations and compared against experimental results in triaxial compression of anisotropic rocks [31, p. 89]. This

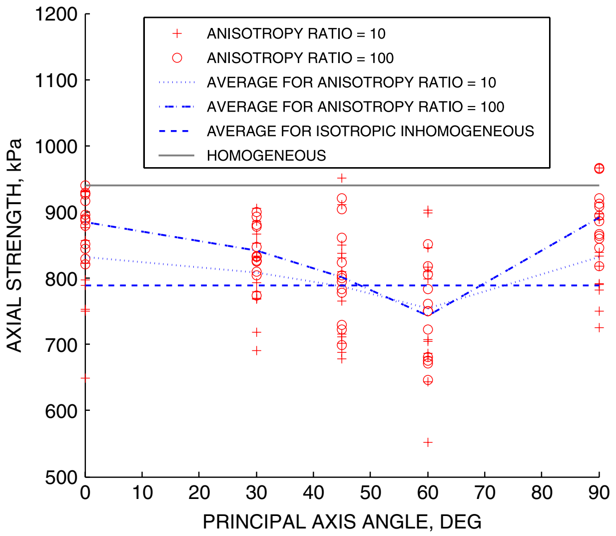

Figure 11. Peak compressive strength for samples of dense sand loaded under plane-strain conditions.

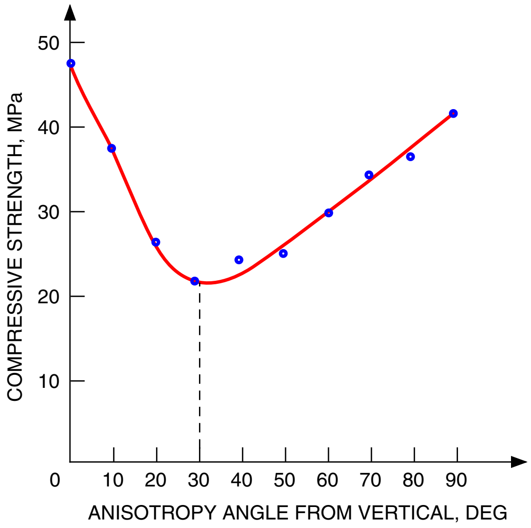

Figure 12. Strength anisotropy in triaxial compression for rocks (after McLamore [30]).

phenomenon is termed ‘strength anisotropy’ in rock mechanics [31]. In particular, the coincidence of the minimum strength, occurring at an orientation of the principal anisotropy of 60° from the horizontal (30° from the vertical), is striking.

Figures 13 and 14 show contours of shear strain and impending shear bands at the instant of failure in normalized samples. The predicted failure plane in the homogeneous sample compares

DOI: 10.1002/nag

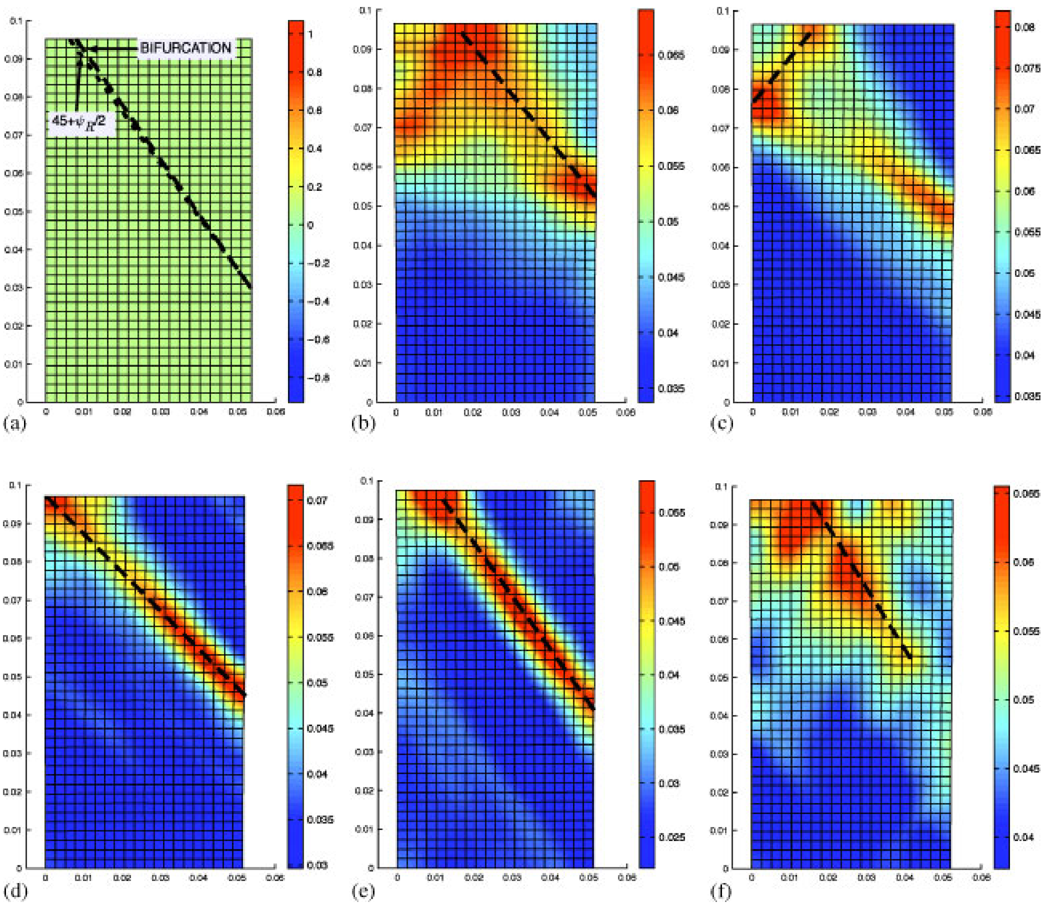

Figure 13. Shear strain contours superimposed on deformed meshes for samples with anisotropy ratio of 10: (a) homogeneous; (b) principal axis 0°; (c) 30°; (d) 45°; (e) 60°; and (f) 90°. Dashed lines highlight shear band orientations.

well with the $45+\psi_R/2$ bound, where ψ_R is the dilatancy angle [32], i.e.

$$\sin\psi_R = \frac{\dot{\varepsilon}_1^{\mathrm{p}}+\dot{\varepsilon}_3^{\mathrm{p}}}{\dot{\varepsilon}_1^{\mathrm{p}}-\dot{\varepsilon}_3^{\mathrm{p}}} \tag{24}$$

The above estimate is attributed to Roscoe [33]. In the case of the homogeneous dense sand sample studied here, the failure angle is approximately 54° for the ‘Roscoe bound’ and 55° from the bifurcation theory (i.e. from the orientation of the normal vector **n** from the impending shear band, see Equation (22)). These orientations are plotted in the homogeneous sample, where the Roscoe estimate is applicable, see Figure 13. Incidentally, the average orientation for all samples ‘tested’ in this work is 55°, regardless of the degree or orientation of the anisotropies. It therefore seems as though the orientation of the failure plane is relatively insensitive to the anisotropies, on average, even though the band orientations do fluctuate from sample to sample,

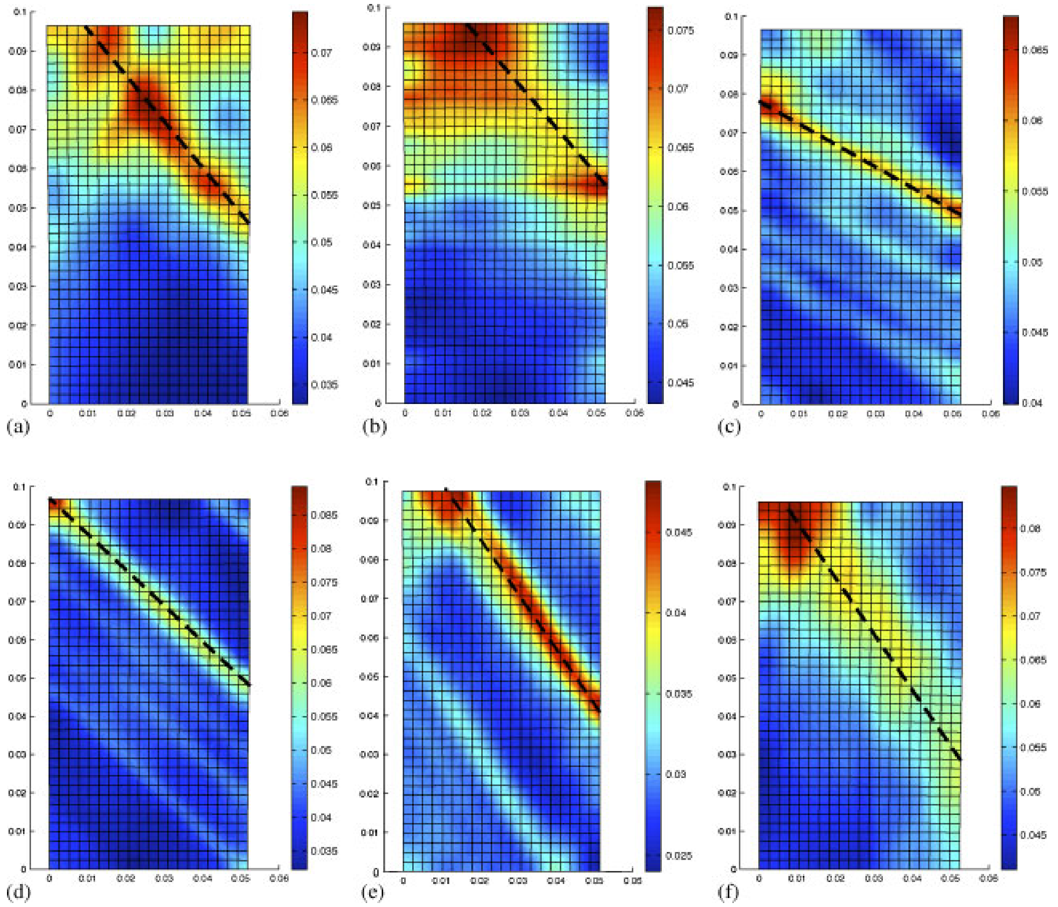

Figure 14. Shear strain contours superimposed on deformed meshes for samples with anisotropy ratio of 100: (a) isotropic; (b) principal axis 0°; (c) 30°; (d) 45°; (e) 60°; and (f) 90°. Dashed lines highlight shear band orientations.

see Figures 13 and 14. On the other hand, samples with higher anisotropy ratios do seem to display more structured failures.

Finally, a sensitivity study on the random field discretization is performed by coarsening the initially 20×40 quad mesh. Two additional meshes are used with 10×20 and 5×10 quadrilateral elements. Coarser discretizations yield more 'homogeneous' samples, which in turn yield higher compressive strengths as depicted in Figure 15 where the load–displacement curves for the normalized sample with $a/b = 100$ and anisotropy orientation of 45° are reported. The initial specific volume for this sample is shown in Figure 16 using a 10×20 mesh (cf. Figure 9(d) with resolution of 20×40 elements). As before, the resolution of all Monte Carlo realization is set to match the finite element discretization. Because the samples share roughly the same porosity values, the curves in Figure 15 lie on top of each other, but predict sharply distinct strengths. The homogeneous response is also plotted for comparison.

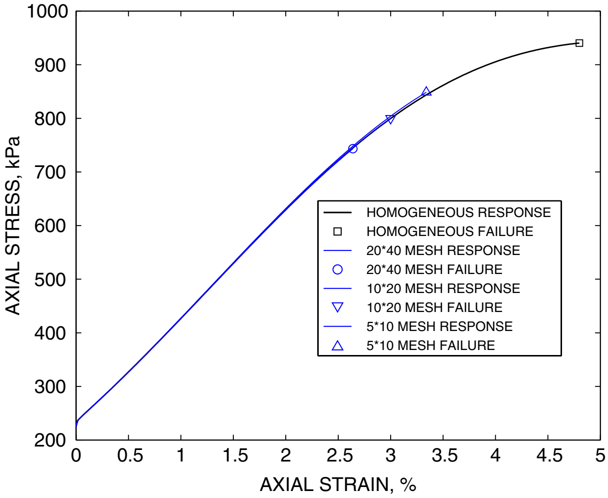

Figure 15. Comparison of force–displacement curves for normalized sample $a/b = 100$ and 45° anisotropy orientation at various levels of discretization.

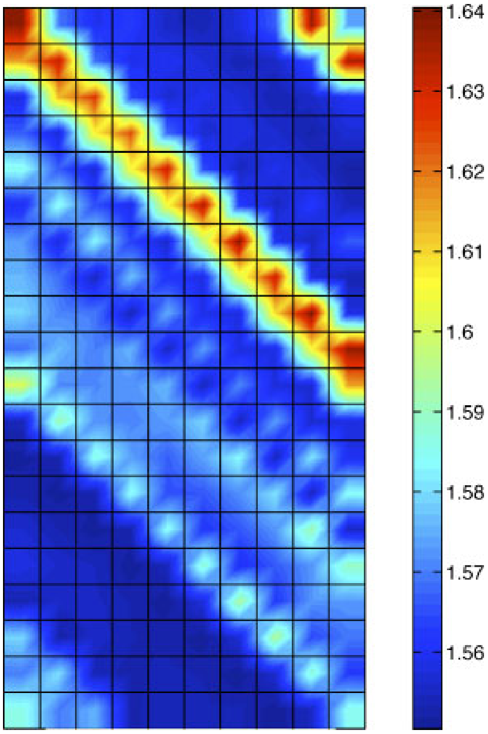

Figure 16. Initial specific volume realization for normalized $a/b = 100$ and 45° anisotropy orientation using a 10×20 mesh.

DOI: 10.1002/nag

The mesh size clearly affects the results of Figure 15, because the discretization affects the ability of the finite element analysis to account for gradients in the random field. Ideally, the finite element size should be smaller than the smallest correlation length (defined by parameters a and b in Equation (19)) in order to capture the intrinsic random field gradients. A second effect arises because the coarse elements include some 'local averaging' over the grid size [34, 35], and this causes a material homogenization that delays failure as the discretization coarsens. Techniques have been developed to account for this local averaging in stochastic finite element analysis, but for the localization phenomenon of interest here it appears to be preferable to use a refined mesh to avoid these complications.

5. CONCLUSIONS

This paper presented a framework for coupling advanced elastoplastic models to reproduce the behavior of granular materials at the meso-scale with state-of-the-art geostatistical tools. The constitutive model utilized is capable of accounting for meso-scale inhomogeneities in the porosity of the material. Ideally, these fluctuations could be obtained using X-ray tomography data but this is rather expensive. For this reason, a stochastic approach was chosen so that material inhomogeneities could be systematically reproduced and their impact in the stability of drained and undrained samples could be analyzed.

Random field models were utilized to characterize porosity values having a specified probability distribution and having spatial correlation within a given specimen. The approach used to characterize porosity values was to specify a probability distribution for porosity values at individual locations. Spatial structure in porosity values was incorporated by simulating spatially correlated Gaussian random fields, and then transforming these fields so that they had the given probability distribution for porosity while retaining an appropriate underlying correlation structure. Both isotropic and anisotropic fields were considered, and for anisotropic fields the severity and orientation of anisotropy were varied systematically. The simulation approach can easily incorporate experimental data that constrains the probability distribution or spatial correlation function. In addition, the approach used for simulating the field is a sequential one, allowing any observations at individual locations in the specimen to be specified at the beginning of the simulation, so that porosity values at other locations are consistent with those observations. For these reasons, combining this approach with experimental work for calibration is a natural extension of this framework.

The simulated specimens were used as input for finite element analyses incorporating the specified constitutive model. Results provided further confirmation that heterogeneities in granular material have an important effect on instabilities at the meso-scale. Parametric studies indicated that axial strength of the specimen is affected by both the degree and orientation of anisotropy in porosity values, with orientation of the anisotropy having a dominant effect, especially when this caused bands of high porosity line up with shear bands.

A total of 150 simulations were performed in this study and the effect of upscaling of porosity fields was looked at closely. It was observed that upscaling delays the predicted onset of localization due to local averaging over mesh elements. These results show the importance of accounting for the meso-scale inhomogeneities and open the door to multi-scale simulations where the effects of inhomogeneities and their interaction with shear bands can be explicitly accounted for.

ACKNOWLEDGEMENTS

The authors are grateful to two anonymous reviewers for their constructive and insightful comments. We are also indebted to Professor Charles Dowding for pointing out the similarity of the results presented in this work with those obtained in anisotropic rocks. Finally, the third author gratefully acknowledges the financial support of a Walter P. Murphy fellowship from Northwestern University.

REFERENCES

1. Alshibli KA, Batiste SN, Sture S. Strain localization in sand: plane strain versus triaxial compression. *Journal of Geotechnical and Geoenvironmental Engineering* (ASCE) 2003; **129**:483–494.
2. Oda M, Takemura T, Takahashi M. Microstructure in shear band observed by microfocus X-ray computed tomography. *Géotechnique* 2004; **54**:539–542.
3. Popescu R, Deodatis G, Nobahar A. Effects of random heterogeneity of soil properties on bearing capacity. *Probabilistic Engineering Mechanics* 2005; **20**(4):324–341.
4. Popescu R, Prevost JH, Deodatis G. Effects of spatial variability on soil liquefaction: some design recommendations. *Géotechnique* 1997; **47**:1019–1036.
5. Griffiths DV, Fenton GA. Probabilistic slope stability analysis by finite elements. *Journal of Geotechnical and Geoenvironmental Engineering* 2004; **130**:507–518.
6. Paice GM, Griffiths DV, Fenton GA. Finite element modeling of settlements on spatially random soil. *Journal of Geotechnical Engineering* 1996; **122**(9):777–779.
7. Been K, Jefferies MG. A state parameter for sands. *Géotechnique* 1985; **35**:99–112.
8. Oda M. Initial fabrics and their relations to mechanical properties of granular materials. *Soils and Foundations* 1972; **12**:17–36.
9. Cundall PA, Strack ODL. A discrete numerical model for granular assemblies. *Géotechnique* 1979; **29**:47–65.
10. Andrade JE, Borja RI. Modeling deformation banding in dense and loose fluid-saturated sands. *Finite Elements in Analysis and Design* 2007; **43**:361–383.
11. Andrade JE, Borja RI. Capturing strain localization in dense sands with random density. *International Journal for Numerical Methods in Engineering* 2006; **67**:1531–1564.
12. Borja RI, Andrade JE. Critical state plasticity, Part VI: Meso-scale finite element simulation of strain localization in discrete granular materials. *Computer Methods in Applied Mechanics and Engineering* 2006; **195**:5115–5140.
13. Ghanem R, Brzakala W. Stochastic finite-element analysis of soil layers with random interface. *Journal of Engineering Mechanics* 1996; **122**(4):361–369.
14. Li C-C, Der Kiureghian A. Optimal discretization of random fields. *Journal of Engineering Mechanics* 1993; **119**(6):1136–1154.
15. Goovaerts P. *Geostatistics for Natural Resources Evaluation*. Oxford University Press: New York, 1997.
16. Jefferies MG. Nor-Sand: a simple critical state model for sand. *Géotechnique* 1993; **43**:91–103.
17. Manzari MT, Dafalias YF. A critical state two-surface plasticity model for sands. *Géotechnique* 1997; **43**:255–272.
18. Argyris JH, Faust G, Szimmat J, Warnke EP, Willam KJ. Recent developments in the finite element analysis of prestressed concrete reactor vessels. *Nuclear Engineering and Design* 1974; **28**:42–75.
19. Gudehus G. Elastoplastische stoffgleichungen fur trockenen sand. *Ingenieur-Archiv* 1973; **42**:151–169.
20. Schofield A, Wroth P. *Critical State Soil Mechanics*. McGraw-Hill: New York, 1968.
21. Cornforth DH. Some experiments on the influence of strain conditions on the strength of sand. *Géotechnique* 1964; **14**:143–167.
22. Shahinpoor M. Statistical mechanical considerations on the random packing of granular materials. *Powder Technology* 1980; **25**:163–176.
23. Phoon KK, Kulhawy FH. Characterization of geotechnical variability. *Canadian Geotechnical Journal* 1999; **36**:612–624.
24. Stanford Center for Reservoir Forecasting. *The Stanford Geostatistical Modeling Software* (*s-gems*), 2006.
25. Rackwitz R. Reviewing probabilistic soils modelling. *Computers and Geotechnics* 2000; **26**:199–223.
26. Phoon KK. Modeling and simulation of stochastic data. *GeoCongress 2006*, vol. 187, Atlanta, Georgia, U.S.A. ASCE: New York, 2006; 17.
27. Rice JA. *Mathematical Statistics and Data Analysis*. Duxbury Press: Belmont, CA, 1995.
28. Baker JW, Faber M. Liquefaction risk assessment using geostatistics to account for soil spatial variability. *Journal of Geotechnical and Geoenvironmental Engineering* 2007, in press.

DOI: 10.1002/nag

29. Andrade JE. A predictive model for static liquefaction. *Géotechnique* 2007, in review.
30. McLamore RT. Strength-deformation characteristics of anisotropic sedimentary rocks. *Ph.D. Thesis*, University of Texas, Austin, TX, 1966.
31. Goodman RE. *Rock Mechanics* (2nd edn). Wiley: New York, NY, 1989.
32. Vermeer PA. The orientation of shear bands in biaxial tests. *Géotechnique* 1990; **40**:223–236.
33. Roscoe KH. The influence of strains in soil mechanics. *Géotechnique* 1970; **20**:129–170.
34. Vanmarcke EH, Grigoriu M. Stochastic finite element analysis of simple beams. *Journal of Engineering Mechanics* 1983; **109**(5):1203–1214.
35. Vanmarcke EH. *Random Fields*, *Analysis and Synthesis*. MIT Press: Cambridge, MA, 1983.